AGU PUBLICATIONS

Geophysical Research Letters

RESEARCH LETTER

10.1002/2017GL072552

Rupture characteristics of the 2016 Meinong earthquake revealed by the back projection and directivity analysis of teleseismic broadband waveforms

Pei-Ru Jian[1], **Shu-Huei Hung**[1], **Lingsen Meng**[2], **and Daoyuan Sun**[3]

[1]Department of Geosciences, National Taiwan University, Taipei, Taiwan, [2]Department of Earth, Planetary, and Space Sciences, University of California, Los Angeles, California, USA, [3]Laboratory of Seismology and Physics of Earth's Interior and School of Earth and Space Sciences, University of Science and Technology of China, Hefei, China

Key Points:

- First high-resolution MUSIC BP image quantifies the rupture properties of the shallow Meinong earthquake that heavily impacted SW Taiwan
- The rupture propagates unilaterally toward the NW and downdip by 17 km over 7 s duration on a shallow NE-dipping blind fault in midcrust
- Directivity effect and strong excitation of sP and reverberations amplify ground shaking and damages to the NW beyond the rupture zone

Supporting Information:

- Supporting Information S1

Correspondence to:

S.-H. Hung,
shung@ntu.edu.tw

Citation:

Jian, P.-R., S.-H. Hung, L. Meng, and D. Sun (2017), Rupture characteristics of the 2016 Meinong earthquake revealed by the back projection and directivity analysis of teleseismic broadband waveforms, *Geophys. Res. Lett.*, *44*, 3545–3553, doi:10.1002/2017GL072552.

Received 11 JAN 2017
Accepted 3 APR 2017
Accepted article online 5 APR 2017
Published online 22 APR 2017

Abstract The 2016 M_w 6.4 Meinong earthquake struck a previously unrecognized fault zone in midcrust beneath south Taiwan and inflicted heavy causalities in the populated Tainan City about 30 km northwest of the epicenter. Because of its relatively short rupture duration and *P* wave trains contaminated by large-amplitude depth phases and reverberations generated in the source region, accurate characterization of the rupture process and source properties for such a shallow strong earthquake remains challenging. Here we present a first high-resolution MUltiple SIgnal Classification back projection source image by using both *P* and depth-phase sP waves recorded at two large and dense arrays to understand the source behavior and consequent hazards of this peculiar catastrophic event. The results further corroborated by the directivity analysis indicate a unilateral rupture propagating northwestward and slightly downward on the shallow NE-dipping fault plane. The source radiation process is primarily characterized by one single peak, ~7 s duration, with a total rupture length of ~17 km and average rupture speed of 2.4 km/s. The rupture terminated immediately east of the prominent off-fault aftershock cluster about 20 km northwest of the hypocenter. Synergistic amplification of ground shaking by the directivity and strong excitation of sP and reverberations mainly caused the destruction concentrated in the area further to the northwest away from the rupture zone.

1. Introduction

On 5 February 2016, a strong devastating earthquake with a moment magnitude (M_w) 6.4 struck the Meinong District of Kaohsiung City in southern Taiwan. Its hypocenter determined by the Central Weather Bureau (CWB) of Taiwan is located at a midcrust depth of 16.7 km beneath the northern tip of the Pingtung Plain, the region covered with the Quaternary alluvial deposits and bounded by the two major faults, the N-S striking Chaochou fault to the east and the NE–SW striking Chishan fault to the west (Figure 1). The U.S. Geological Survey USGS CMT (centroid moment tensor) solution of the main shock and distribution of its aftershocks reported by the CWB suggest that the earthquake slipped on a shallow NE-dipping fault plane striking N61°W with both left-lateral strike slip and thrust motions (Figure 1). Amplification of ground motion by sediment reverberations coupled with local site effects have been blamed for partly causing the collapse of high-rise buildings and severe fatalities in Tainan City, about 20 km northwest of the epicenter.

For the last nearly three centuries, several historically documented events with similar or larger magnitudes had rattled the Tainan area which also resulted in substantial damages and casualties. The two recent ones occurring in very close proximity to the 2016 Meinong earthquake are the 1946 Hsinhua and 1964 Baihe earthquakes located about 40 km to the northwest and 30 km to the north, respectively [*Cheng and Yeh*, 1989]. After about 45 years of seismic quiescence, strong earthquakes with magnitude greater than 6 started to reactivate in the vicinity, including the 2010 M_w 6.2 Jiashian and 2012 M_w 6.3 Wutai earthquakes that struck 25–30 km deep east and southeast of Meinong on the blind faults beneath the southern Central Mountain Range [*Hsu et al.*, 2011; *Chan and Wu*, 2012; *Lee et al.*, 2013]. As revealed by the earthquakes in 1990–2015 from the CWB catalog, the Meinong event occurred in an NW-SE trending linear zone of background seismicity with no clear link to any known faults. This linear feature delineates the boundary between the seismically active, rugged hilly terrain to the north and east, and the Pingtung Plain to the south with extremely low seismicity. Two prominent aftershock clusters were triggered near the source region within hours to days after the main shock. The one nearest to the hypocenter was distributed at 10–20 km depth along the linear

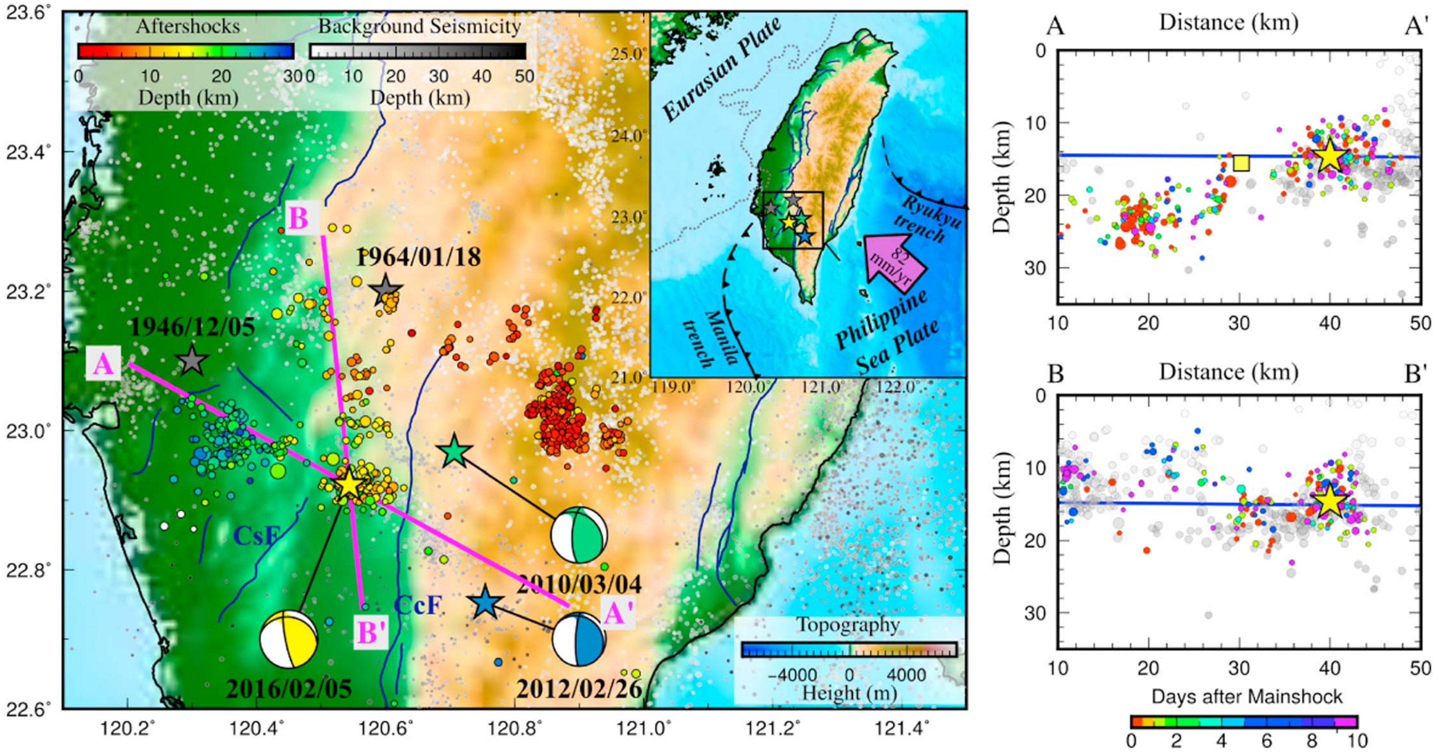

Figure 1. (a) Tectonic setting of the Meinong earthquake outlined by a black box in the inset map showing the plate configuration around Taiwan. The stars show earthquakes with $M_w > 6.0$ recorded in this area during the instrumentation era, with the focal mechanisms from the BATS database. The color and gray circles denote the aftershocks within 10 days after the main shock and background seismicity with $M_L > 2.0$ from the CWB catalog, with size and color scaled by magnitude and depth, respectively. (b) Projection of all the earthquakes located within 5 km on either side of the AA′ and BB′ cross sections parallel to the strikes of the two nodal planes shown in Figure 1a, where the yellow star and the square mark the hypocenter and terminus of the rupture from our BP image.

background seismic zone as mentioned above and the other more concentrated deeper at 20–30 km depth to the WNW about 20–30 km from the source. These two clusters appear to be aligned on an NW-SE trend parallel to the strike of one of the nodal planes inferred from the CMT of the main shock but separated by a seismic gap in between. Additionally, fewer aftershocks, in spite of being quite sparse and scattered, seem to run roughly parallel to the strike of the other nodal plane (N174°E) and steep topographic front.

In spite that the fault plane orientation, average slip vector, and rupture area of an earthquake can be crudely determined from the CMT mechanism, aftershocks, and surface field observations, tracking the details of the rupture process is of essential importance for comprehensively understanding the source characteristics and consequent impacts of a destructive event. A back projection (BP) method using high-frequency (HF) teleseismic body waves recorded at large-aperture dense arrays is well suited for this purpose, as it has been demonstrated effective in imaging the space-time evolution of radiated energy with no need of much a priori knowledge about source parameters [*Ishii et al.*, 2007]. Here we employ the multitaper-MUltiple SIgnal Classification (MUSIC) BP technique [*Meng et al.*, 2010] to illuminate coherent radiation sources through time for tracking the rupture process of the Meinong earthquake. The obtained image would facilitate the identification of the asperity on the previously unknown fault zone and estimation of important source parameters such as rupture speed, length, and direction. Using broadband waveforms recorded globally and modeled synthetics, we further verify our BP results through the directivity and source radiation analyses.

2. Methods and Data

In principle, the BP method tracks the rupture front of an earthquake by extracting coherent seismic arrivals radiated from common source points and propagating them backward in time to the positions of the respective radiators [*Ishii et al.*, 2007; *Koper et al.*, 2011]. Practically, there are various ways to perform the reverse-time source imaging, such as the time domain stacking [*Ishii et al.*, 2007], frequency domain compressive sensing [*Yao et al.*, 1982], and MUSIC (MUltiple SIgnal Classification) [*Meng et al.*, 2010, 2011, 2012b].

Because a seismic signal is inherently nonstationary and there exists a trade-off between its arrival time and traveling distance, the drift of the stacked energy over time toward the direction to the array is inevitable for the BP results [*Ishii et al.*, 2007; *Koper et al.*, 2011]. This so-called swimming artifact can be much mitigated by the MUSIC to enhance the image resolution [*Meng et al.*, 2012a]. The method estimates the covariance matrix of waveforms for every sliding time window and sampling frequency by a multitaper approach [*Thomson*, 1986] and projects it into the signal and noise subspace [*Schimdt*, 2002]. The steering vector consists of the frequency domain phase shifts at each station to correct for the arrival-time shifts of the signals from each candidate source relative to the hypocenter. The direction of arrival associated with the strongest radiator is determined by the maximum amplitude of the frequency-average MUSIC pseudospectrum, defined as the inverse of the projection of the steering vector onto the noise subspace [*Meng et al.*, 2010].

In this study, we combine the high-resolution MUSIC BP and directivity analysis to explore the rupture process of the Meinong earthquake in detail by using global teleseismic broadband records. The vertical velocity waveforms filtered at 0.5–1.5 Hz from two large and dense seismic networks in Europe (EU) and Australia (AU) are first aligned on the initial *P* arrivals as the onset (zero time) of the rupture (Figure S1 in the supporting information). By choosing overlapping sliding windows of appropriate length, we perform the multitaper cross-spectral estimation of the windowed signals for the subspace projection analysis. Nodes of a 50×50 km^2 grid mesh centered at the hypocenter with a 2 km spacing along the strike and dip of the presumed fault plane are specified as candidate source radiators. We test two plausible scenarios of the rupture propagating on either one of two conjugate nodal planes derived from the USGS CMT. The results favor the shallow NE-dipping one striking N61°W as the rupture plane. We also conduct the joint back projection of *P* and depth phase sP on a 3-D volume without a priori specifying the fault plane. Similar to the 2-D results, the combined 3-D image seen from the AU array suggests the rupture propagating subhorizontally toward northwest in favor of the NW-striking nodal plane as the fault plane, though there exists larger uncertainties in the imaged radiator locations (see Figure S2 for details).

3. Back Projection Source Image

Figure 2 summarizes our BP results by using *P* and sP wave trains from the AU and EU arrays. We test different lengths of the sliding window shifted in every second and choose 3 s, about twice of the dominant period of the filtered *P* pulses, to achieve both the optimal time resolution and stability of the BP images. The rupture process is illuminated by the strongest radiators in every 2 s projected on the map. The respective peak amplitude of the MUSIC pseudospectrum varying with time is also shown as the apparent source time function, similar to the maximum amplitude of the stacked energy obtained in the time domain BP method.

In Figure 2a, we show the BP results obtained with ~20 s long wave trains starting from the aligned *P* arrivals. The MUSIC pseudospectrum observed at the AU and EU arrays grossly resembles the displacement waveforms shown in Figure 3b, indicating two major episodes of source energy release. Each episode begins with an ~5–7 s long, stronger radiation burst followed by a rapid decay afterward, but the peak and duration observed from the AU array appear later and longer by about 2 s than those from the EU array. In the first episode, except for the last 2–3 s during which the normalized amplitude of the MUSIC pseudospectrum at the EU drops rapidly to very small values (<-3 dB), the radiators seen by both the arrays show the predominance of a unilateral rupture propagating primarily toward the NW and slightly downdip. Though the AU compared to the EU array has a less dense station coverage, the shorter epicentral distance and favorable azimuth opposite to the rupture direction lead to the recorded waveforms having longer duration and higher coherence and signal-to-noise ratios. The AU image thus gives preferable spatiotemporal resolution for more robust estimates of the rupture length, speed, direction, and duration. The following investigation of the main rupture features mostly rely on the AU results.

Despite some minute differences probably due to the source radiation pattern and directivity effect, the overall HF radiators reveal fairly consistent space-time distributions during the first 5–8 s. In contrast, during the second episode there are large discrepancies in the radiator locations between the two arrays, even though the apparent source time functions and displacement waveforms of the two episodes are similar. The EU radiators emitted between 10 and 14 s are found to move further northwest about 20 km from the epicenter above the deeper off-fault aftershock cluster, while the AU radiators are shifted eastward in the reverse direction to the previously ruptured area. We notice that these inconsistent radiators are mainly back

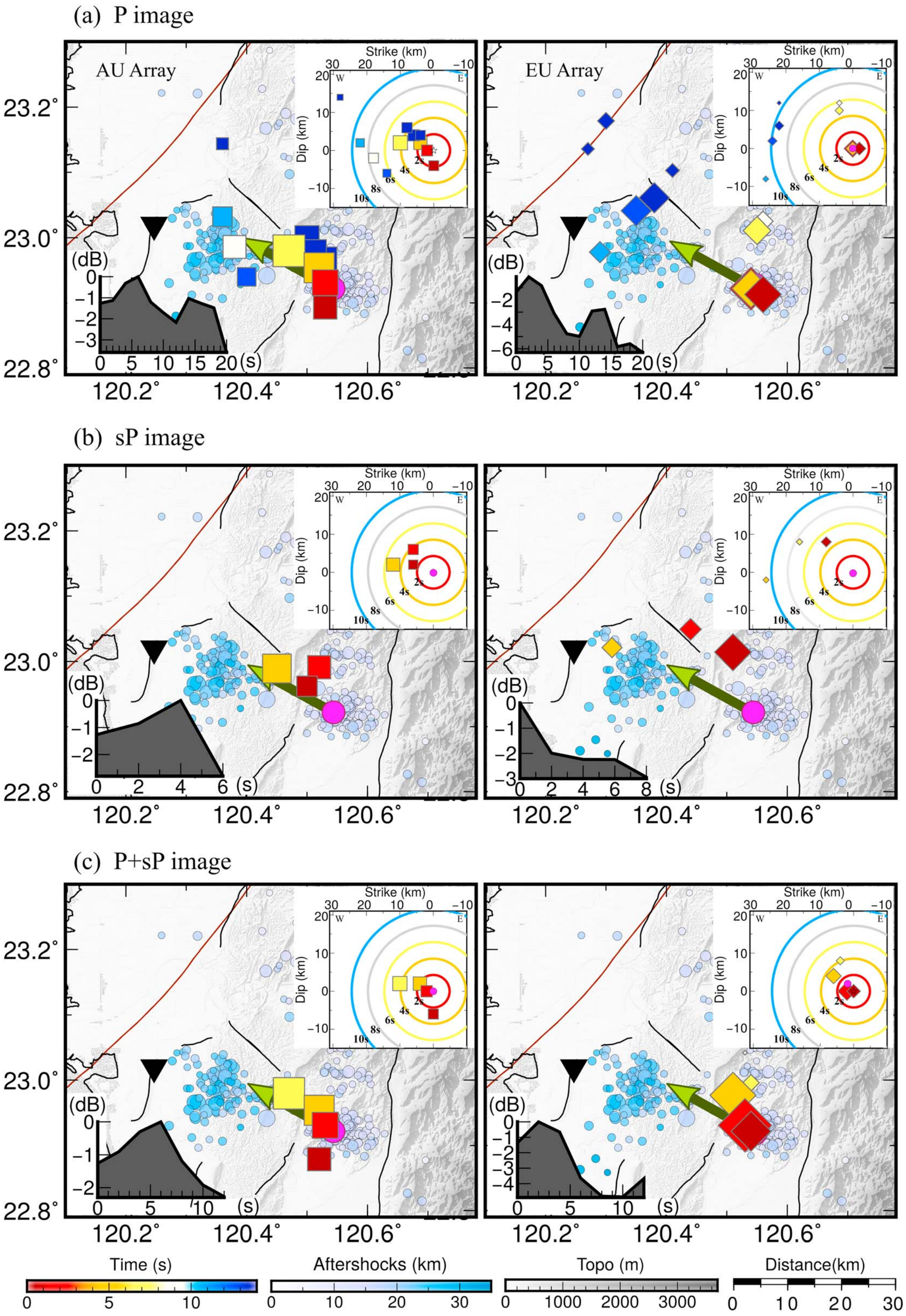

Figure 2. Spatiotemporal distributions of the strongest radiators imaged with the MUSIC BP by using (a) ~20 s *P*, (b) ~6 s sP, and (c) both *P* and sP waves at the AU (square) and EU (diamond) arrays, with symbol size and color scaled by the radiation strength and time elapsed. The green arrows show the rupture direction and length from the directivity analysis and the inverted triangles the most damaged Tainan area. (top right) The distances of the radiators from the hypocenter along the strike and dip, with concentric circles for the rupture fronts at specific times assuming a rupture speed of 2.5 km/s. (bottom left) The peak amplitudes of the normalized MUSIC pseudospectrum in decibel (dB) over time.

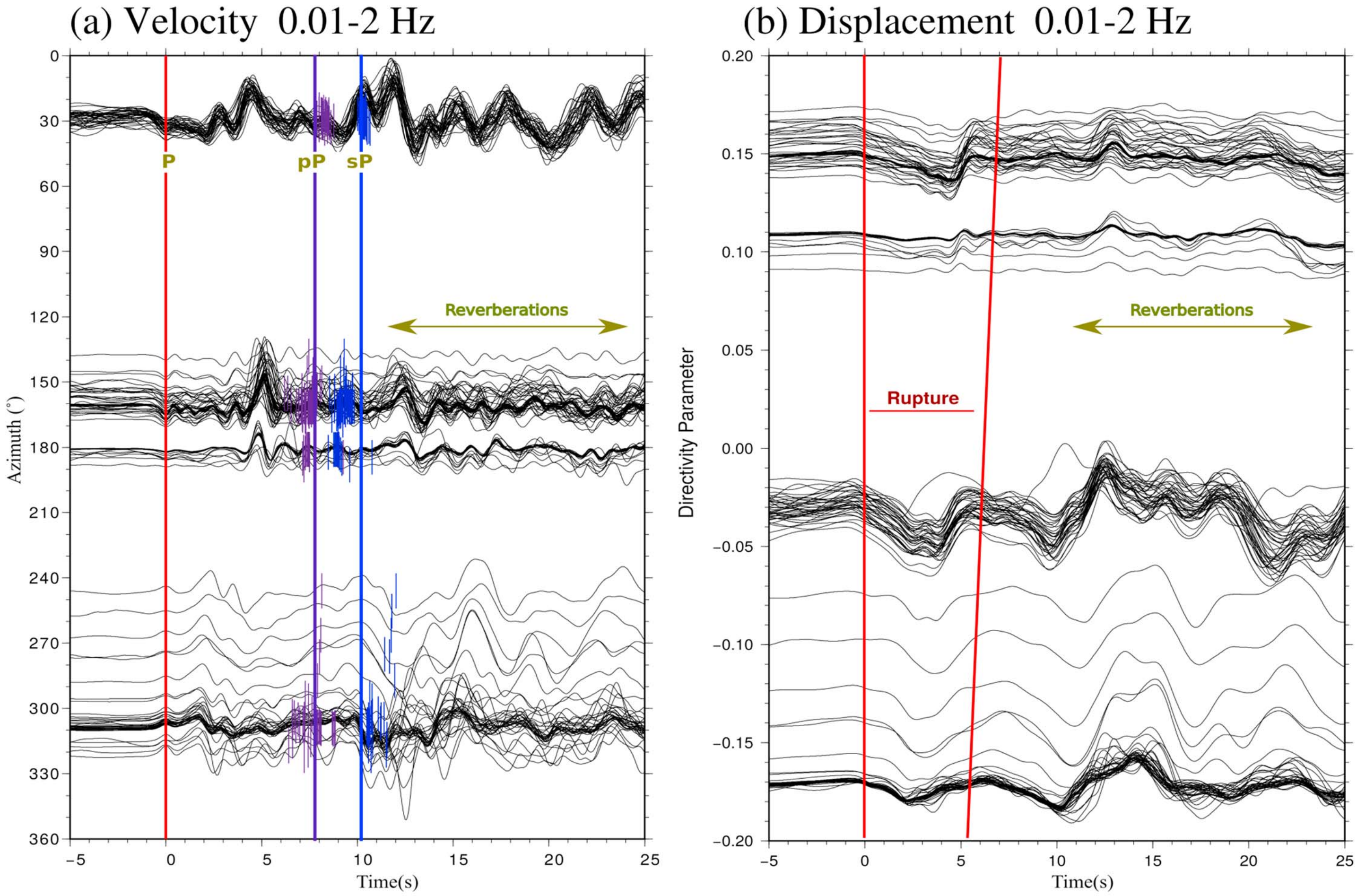

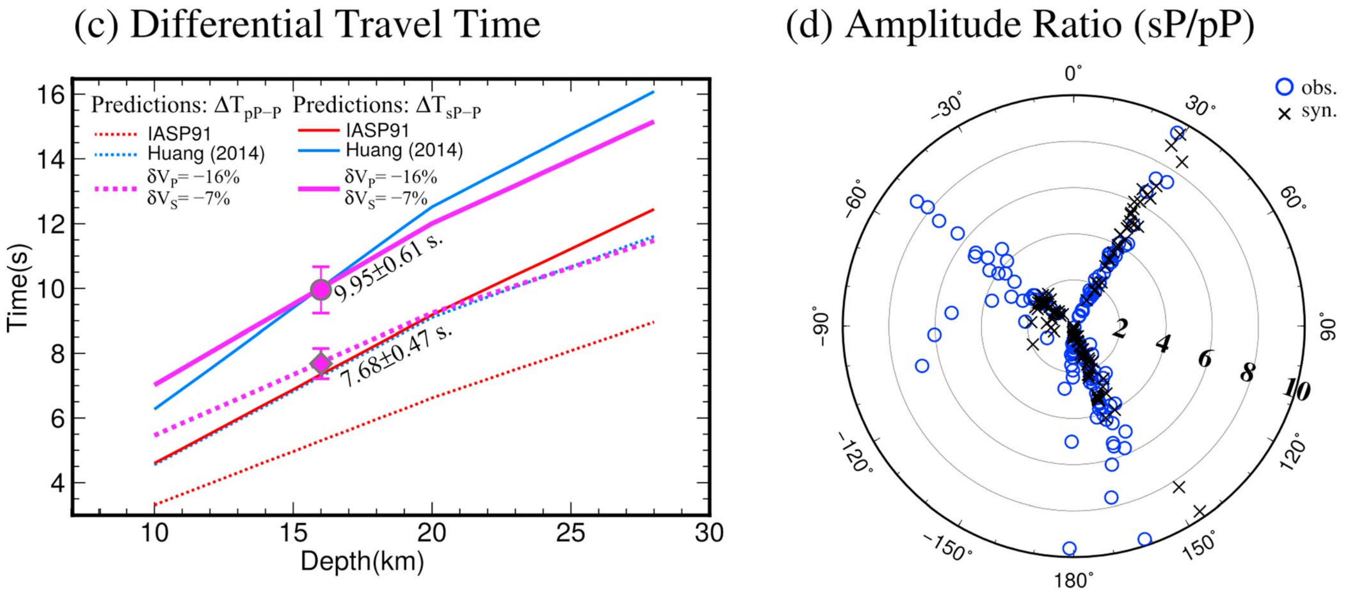

Figure 3. (a) Teleseismic velocity waveforms at 0.01–2 Hz varying with azimuth. The red, purple, and blue lines mark the aligned *P* and average hand-picked pP and sP arrivals (thin bars), respectively. (b) Displacement waveforms varying with directivity parameter, with the rupture duration marked by red lines. Note that the positive *P* wave polarity has been reversed. (c) Differential pP-*P* and sP-*P* travel times varying with focal depth. The red, blue, and pink lines indicate the pP-*P* and sP-*P* times predicted for three 1-D models from IASP91, the local tomography model [*Huang et al.*, 2014], and our estimates that fit the observed differential times for a 16 km deep event. The circles with error bars show the averages and standard deviations of the picked pP-*P* and sP-*P* times. (d) Comparison of the observed (circle) and predicted (cross) sP/pP amplitude ratios varying with azimuth.

projected from the second major pulses which have the arrival-time moveouts and amplitudes comparable to the first ones (Figure 3b). Considering the hypocentral depth of ~16 km and relative short rupture duration typical for the M_w 6.4 event, we speculate that these late-arriving pulses originate from the surface-reflected depth phases, pP and sP.

To corroborate this speculation, we manually pick the onset times and peak amplitudes of the pP and sP phases on the vertical velocity component of teleseismic waveforms filtered at 0.01–2 Hz (Figure 3a). To help reliably identify and characterize the observed depth phases from the variations in waveform polarity and amplitude with azimuth, we calculate the corresponding synthetic seismograms as reference (Figure S3) by the frequency-wave number method [*Zhu and Rivera*, 2014], assuming a 1-D local crustal velocity structure (Figure S4b) and a point source with the USGS CMT focal mechanism and CWB located hypocenter. We also perform an *N*th-root vespagram analysis [*Rost and Thomas*, 2015] to estimate the horizontal slownesses of the coherent arrivals observed at the two dense arrays with nearly perpendicular azimuths (see details in Figure S5). The slownesses determined by the maxima of the stacked energy agree with the theoretical values for *P* and sP, but their arrival times are considerably delayed compared to those predicted by IASP91 model. The observed differential sP-*P* and pP-*P* times and amplitude sP/pP ratios are then compared with those predicted by the synthetics. As long as the ratio of *P* to *S* velocity does not vary significantly, the travel time difference between sP and pP with similar ray paths is not susceptible to shallow velocity structures near the source and can be used to constrain the focal depth. The average differential sP-pP time from our picking is 2.27 s consistent with the reported depth of ~17 km. Compared to those predicted by the global IASP91 model, the observed sP-*P* and pP-*P* times are substantially delayed by 2–2.4 s. Besides, the sP phases observed at the azimuth of AU (~140°) and EU (~310°) stations persistently arrive earlier and later, respectively, than the average picked time of ~10 s after *P*. These arrival-time changes with azimuth are mostly ascribed to lateral velocity heterogeneity around the hypocenter. The 3-D local tomography model [*Huang et al.*, 2014] indicates that the earthquake occurs in the midcrust overlain by a 10–15 km thick sedimentary layer with low *P* and *S* wave velocities and in transition to a relatively faster upper crust to the east beneath the southcentral mountain range (Figure S3). To reconcile the average ~2 s delay of the observed depth phase arrivals, we replace the crustal velocity model in IASP91 by the layer-averaged tomography model and vary the velocities in the upper and middle crustal layers. We find that the average *P* and *S* velocities have to be respectively reduced by 16 ± 4% and 7 ± 7% relative to the 1-D local model (Figure 3c). The radiated seismic energy propagating through the shallow low-velocity layer generates strong reverberations seen at all the stations, with slowly decaying amplitude and long duration over 10 s emerging after the sP (Figure 3a). As the amplitudes of high-frequency waves are strongly influenced by scattering from heterogeneity, the observed sP/pP ratios exhibit considerable scattered variations with azimuth unmodeled by the 1-D synthetics. Despite this, the amplitudes estimated from the 1-D synthetics can properly predict the large, less scattered ratios observed in the NE and SE azimuths, where the pP and sP waves travel eastward through the upper crust covered with less sediments.

As we confirm the phase arriving at ~10 s after *P* is mainly the sP, we separate these two phases and synchronize their respective onset times to conduct the BP imaging individually. The time-evolving radiators constrained from the *P* and sP waves at the AU array are consistent. The sP waves propagating northwest through the very thick low-velocity layer to the EU stations and more contaminated by reverberations are less coherent, resulting in the much weaker radiators. Even so, compared to those using the longer *P* wave trains mixed with the depth phases, the rupture patterns obtained with the sP only at the two arrays become more consistent with each other (Figure 2b).

From the previous study [*Kiser et al.*, 2011] and our exercises using both the observed and synthetic data, combining the BP results from multiple phases with different takeoff angles can help improve the image resolution and reduce the uncertainties of the radiator locations for further evaluation of the rupture parameters. Two synthetic tests are presented in Figures S6 and S7 to demonstrate the capability of our joint *P* and sP BP imaging in restoring assumed source scenarios with various rupture extent and duration. In Figure 2c, we integrate the *P* and sP obtained rupture images by summing linearly the amplitudes of the respective MUSIC pseudospectrum for each candidate source and given time interval. Those at which the summed amplitudes reach the maxima are identified as the strongest radiators and the corresponding peak amplitudes of the MUSIC pseudospectrum as the apparent source time function (Figure 2c). The summed AU image indicates that the rupture is initially stagnant nearest the hypocenter at 0–2 s, then propagates toward

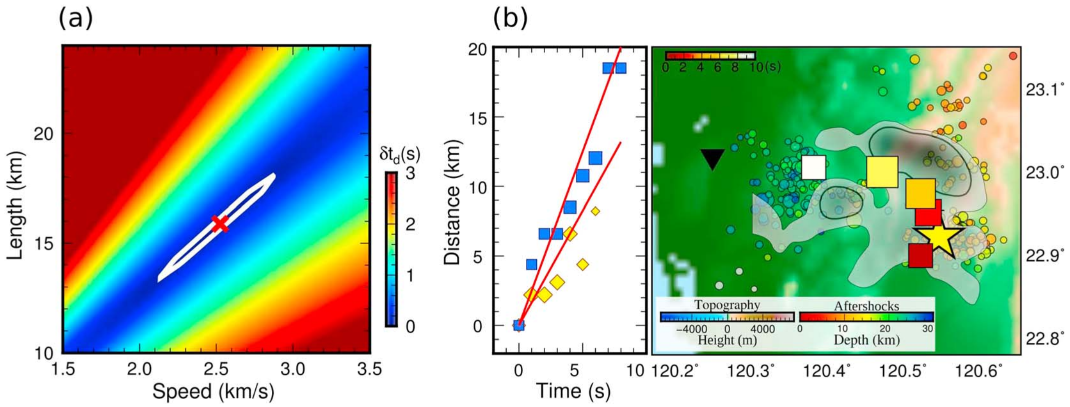

Figure 4. (a) The rupture speed (*v*) and length (*L*) (red cross) that best fit the observed rupture duration (t_d) at the AU, EU, and NA stations from the directivity analysis. The color image shows the RMS misfit between the observed and predicted t_d (white ellipse for RMS = 0.1 s). (b) (left) Propagation distance of the time-evolving radiators from the hypocenter at the AU (square) and EU (diamond) arrays. The average *v* estimated by the slope of each least squares fit line is 2.5 and 1.6 km/s, respectively. (right) Comparison between the radiator locations (square) from the AU image and cumulative slip distribution from the finite-fault model [*Lee et al.*, 2016], with light and dark gray shaded areas showing the slip exceeding 15% and 30% of the maximum value. The other symbols are explained in Figure 1a.

the northwest and slightly downdip between 2 and 6 s and turns more horizontally at 6–8 s. This rupture scenario agrees with the aftershock distribution in the vicinity of the hypocenter which forms a linear trend roughly parallel to the strike of the rupture plane (Figure 1b). The rupture extent spans about 10 km along the strike and 7 km along the downdip direction and ends at the eastern periphery of the off-fault aftershock zone located ~20–25 km northwest of the epicenter. The average rupture speed is about 2.4 km/s by taking a total rupture length of ~17 km and duration of ~7 s.

4. Rupture Directivity and Source Radiation Analysis

To further verify our BP results, we conduct the directivity analysis by using all the global teleseismic broadband records. Assuming a simple kinematic source model for an earthquake rupturing on a rectangular fault of finite length *L*, the apparent rupture duration, t_d, observed from a teleseismic *P* wave at azimuth, φ, is expressed as $t_d = \frac{L}{v} - \frac{L\cos(\varphi-\varphi_r)\sin i_h}{c}$, where *c* is the *P* wave velocity, *v* the rupture speed, i_h the takeoff angle, and φ_r the rupture azimuth. If the Meinong earthquake ruptured with multiple subevents, by arranging the waveforms as a function of directivity parameter defined as $-\frac{\cos(\varphi-\varphi_r)}{c}$ [*Zhan et al.*, 2011; *Park and Ishii*, 2014], we would observe the multiple coherent arrivals aligned along the straight lines with different slopes. The rupture duration, $\frac{L}{v}$, for each subevent is equal to the intercept of the line crossing the zero directivity parameter. Considering that the rupture propagates predominantly toward N61°W as seen in the BP image, we display the displacement waveforms aligned on the onset *P* arrivals as a function of directivity parameter (Figure 3b). The rupture directivity toward the NW is clearly evidenced by the time duration of the first pulse linearly increasing with the directivity parameter. Besides, the onset times of the second pulses seem to be aligned on the same moveout as the *P*. Though the amplitudes of these two pulses vary differently with the directivity parameter, the overall waveform shapes are very similar with one single dominant peak, further implying that these two seismic pulses originate from the same rupture process.

We determine the apparent rupture duration, t_d, from the length of the first pulse, which is the shortest (5.3 s) toward the EU (azimuth ~303°), the intermediate (6.3 s) toward the North America (NA) (azimuth ~30°), and the longest (7.4 s) toward the AU (azimuth ~138°). To obtain a quantitative estimate of the rupture speed *v* and length *L*, we vary *v* and *L* to minimize the root-mean-square misfit between the observed and predicted t_d at the three azimuths (Figure 4a). The resulting *v* and *L* are 16 ± 4 km and 2.0 ± 0.5 km/s, respectively, consistent with those estimated from the BP images. According to the empirical scaling relation between seismic moment and fault length [*Leonard*, 2010], the fault length of an interplate strike-slip earthquake with magnitude 6.4–6.6 is about 13.6–17.2 km. Our estimate for the M_w 6.4 Meinong event falls within this reasonable range.

5. Discussions and Conclusions

The finite-fault model of *Lee et al.* [2016] shows that the Meinong earthquake has two slip asperities with an overall area of ~25 × 25 km^2 and the moment release with a total duration of ~16 s. However, our BP and directivity analyses yield the considerably shorter rupture length (~17 km) and duration (~7 s), with the strong directivity pointing more toward the northwest than the fault strike of N79°W assumed in their finite-source model. The rupture extent constrained by our AU image is partially overlapped with the first asperity which starts with a small patch near the hypocenter at 0–2 s and during 2–8 s moves downdip about 18 km and then horizontally about 10 km to the west (Figure 4b). The resulting moment rate function has the prominent peaks at 3–5 s, similar to the strongest radiation burst which reaches the maximum amplitude of the MUSIC pseudospectrum in the AU image (Figure 2c).

The second asperity developed after 9 s is located immediately west of the first one but shifted to the shallower depth of ~15 km above the off-fault aftershock cluster. This smaller slip patch is very close to the radiator emitted at 10 s in our AU image (white square in Figure 4d), where the sP and reverberating wave trains are considered as part of the direct *P* in the BP imaging. It results in a continuously westerward-propagating rupture with a much longer rupture length and duration atypical for the M_w 6.4 event. We find that the direct *P* and depth phases of the shallow Meinong event would overlap each other if the lowpass cutoff frequency chosen to filter the waveforms at the AU stations is too low at 1 Hz as that used for the finite-fault inversion. This may explain that the moment magnitude of several earthquakes with M_w = 6.0–6.5 in Taiwan tends to be overestimated by the finite-fault models compared to the global CMT solutions, and so do the rupture area and source duration.

Combing the BP results with constraints from the directivity and source radiation pattern, we conclude that the rupture does not reach the depth shallower than 15 km nor beyond the off-fault aftershock cluster about 20–30 km northwest of the hypocenter. The Meinong earthquake happened to rupture toward the NW azimuth close to the maximum *S* wave excitation. The radiated energy propagating through the very thick, low-velocity layer west of the epicenter generated strong reverberations. Synergistic amplification of ground motion by strong directivity and excitation of sP and reverberations mainly caused the destruction in Tainan further to the NW from the rupture zone. Our analysis demonstrates that the source parameters such as the rupture extent and duration especially for strong shallow earthquakes with $M_w < 7$ can be overestimated if late-arriving *P* wave energy included in the BP imaging and finite-fault inversion are dominated by depth phase and reverberant energy.

Acknowledgments
We thank the Australian National Seismograph Network operated by Geoscience Australia (http://www.ga.gov.au), ORFEUS (http://www.orfeus-eu.org), and IRIS DMC (http://ds.iris.edu) for seismic data and USGS (http://earthquake.usgs.gov), BATS (http://bats.earth.sinica.edu.tw), and CWB of Taiwan (http://www.cwb.gov.tw) for the moment tensors and hypocenters of earthquakes used in our study. C.-H. Chang and S.-J. Lee provide us the relocated aftershocks and finite-fault model. The comments from two anonymous referees and Editor J. Ritsema help improve the manuscript. The work was supported by the Ministry of Science and Technology (MOST) of Taiwan under grants 104-2116-M-002-002 and 105-2116-M-002-006.

References

Chan, C.-H., and Y.-M. Wu (2012), A seismicity burst following the 2010 *M* 6.4 Jiashian earthquake—Implications for short-term seismic hazards in southern Taiwan, *J. Asian Earth Sci.*, *59*, 231–239.

Cheng, S. N., and Y. T. Yeh (1989), Catalog of the Earthquakes in Taiwan from 1604 to 1988 [in Chinese], *IES-R-661*, 8-10, 255 pp., *Inst. Earth Sci.*, Taipei.

Hsu, Y.-J., S.-B. Yu, L.-C. Kuo, Y.-C. Tsai, and H.-Y. Chen (2011), Coseismic deformation of the 2010 Jiashian, Taiwan earthquake and implications for fault activities in southwestern Taiwan, *Tectonophysics*, *502*(3–4), 328–323.

Huang, H.-H., Y.-M. Wu, X. Song, C.-H. Chang, S.-J. Lee, T.-M. Chang, and H.-H. Hsieh (2014), Joint Vp and Vs tomography of Taiwan: Implications for subduction-collision orogeny, *Earth Planet. Sci. Lett.*, *392*, 177–191.

Ishii, M., P. M. Shearer, H. Houston, and J. E. Vidale (2007), Teleseismic *P* wave imaging of the 26 December 2004 Sumatra-Andaman and 28 March 2005 Sumatra earthquake ruptures using the Hi-net array, *J. Geophys. Res.*, *112*, B11307, doi:10.1029/2006JB004700.

Kiser, E., M. Ishii, C. H. Langmuir, P. M. Shearer, and H. Hirose (2011), Insights into the mechanism of intermediate-depth earthquakes from source properties as imaged by back projection of multiple seismic phases, *J. Geophys. Res.*, *116*, B06310, doi:10.1029/2010JB007831.

Koper, K. D., A. R. Hutko, T. Lay, C. J. Ammon, and H. Kanamori (2011), Frequency-dependent rupture process of the 2011 *M*(*w*) 9.0 Tohoku earthquake: Comparison of short-period *P* wave backprojection images and broadband seismic rupture models, *Earth Planets Space*, *63*, 599–602, doi:10.5047/eps.2011.05.026.

Lee, S.-J., L. Mozziconacci, W.-T. Liang, Y.-J. Hsu, W.-G. Huang, and B.-S. Huang (2013), Source complexity of the 4 March 2010 Jiashian, Taiwan, Earthquake determined by joint inversion of teleseismic and near field data, *J. Asian Earth Sci.*, *64*, 14–26.

Lee, S.-J., T.-Y. Yeh, and Y.-Y. Lin (2016), Anomalously large ground motion in the 2016 M_L 6.6 Meinong, Taiwan, earthquake: A synergy effect of source rupture and site amplification, *Seismol. Res. Lett.*

Leonard, M. (2010), Earthquake fault scaling: Self-consistent relating of rupture length, width, average displacement, and moment release, *Bull. Seismol. Soc. Am.*, *100*(5A), 1971–1988, doi:10.1785/0120090189.

Meng, L., A. Inbal, and J.-P. Ampuero (2011), A window into the complexity of the dynamic rupture of the 2011 M_w 9 Tohoku-Oki earthquake, *Geophys. Res. Lett.*, *38*, L00G07, doi:10.1029/2011GL048118.

Meng, L., J.-P. Ampuero, A. Sladen, and H. Rendon (2012a), High-resolution backprojection at regional distance: Application to the Haiti *M*7.0 earthquake and comparisons with finite source studies, *J. Geophys. Res.*, *117*, B04313, doi:10.1029/2011JB008702.

Meng, L., J.-P. Ampuero, Y. Luo, W. Wu, and S. Ni (2012b), Mitigating artifacts in back-projection source imaging with implications for frequency-dependent properties of the Tohoku-Oki earthquake, *Earth Planets Space*, *64*(12), 1101–1109, doi:10.5047/eps.2012.05.010.

Meng, L., J.-P. Ampuero, and R. Bürgmann (2014), The 2013 Okhotsk deep-focus earthquake: Rupture beyond the metastable olivine wedge and thermally controlled rise time near the edge of a slab, *Geophys. Res. Lett.*, *41*, 3779–3785, doi:10.1002/2014GL059968.

Park, S., and M. Ishii (2015), Inversion for rupture properties based upon 3-D directivity effect and application to deep earthquakes in the Sea of Okhotsk region, *Geophys. J. Int.*, *203*(2), 1011–1025.

Rost S., and C. Thomas (2002), Array seismology: Methods and applications, *Rev. Geophys.*, *40(3)*, 1008, doi:10.1029/2000RG0001000.

Schimdt, R. O. (1986), Multiple emitter location and signal parameter estimation, *IEEE Trans. Antennas Propag.*, *34*(3), 276–280.

Thomson, D. J. (1982), Spectrum estimation and harmonic analysis, *Proc. IEEE*, *70*(9), 1055–1096.

Yao, H., P. Gerstoft, P. M. Shearer, and C. Mecklenbräuker (2011), Compressive sensing of the Tohoku-Oki M_w 9.0 earthquake: Frequency-dependent rupture modes, *Geophys. Res. Lett.*, *38*, L20310, doi:10.1029/2011GL049223.

Zhan, Z., H. Kanamori, V. C. Tsai, D. V. Helmberger, and S. Wei (2014), Rupture complexity of the 1994 Bolivia and 2013 Sea of Okhotsk deep earthquakes, *Earth Planet. Sci. Lett.*, *385*, 89–96, doi:10.1016/j.epsl.2013.10.028.

Zhu, L., and L. A. Rivera (2002), A note on the dynamic and static displacements from a point source and in multilayered media, *Geophys. J. Int.*, *148*, 619–627.